Towards a Few-Degree Calorimeter

Bridging the Q^2 Gap to Support the Quest for Gluon Saturation

Miguel Arratia (contact), Barak Schmookler, Sebouh Paul, Weibin Zhang
University of California, Riverside

July 14, 2023

Abstract

Measuring the region $0.1 < Q^2 < 1.0$ GeV^2 is essential to support research on gluon saturation. Recent studies have revealed that covering this region at the highest beam energies is not feasible with standard approaches, resulting in the so-called Q^2 gap. A calorimeter near the beam pipe with high granularity has the potential to solve this issue by maximizing acceptance and yielding excellent e/h discrimination through shower shapes. We propose an R&D program to develop a SiPM-on-tile tungsten-scintillator calorimeter that can bridge the Q^2 gap and provide highly granular 5D shower reconstruction. By the end of this proposed plan, we will have established a concrete design and have characterized a prototype under beam conditions.

Contents

1 Motivation

The technology currently used to cover the smallest electron-scattering angles with the central detector consists of lead-tungsten crystals. These crystals provide unparalleled energy resolution, which enhances the performance in reconstructing the Deep-Inelastic Scattering (DIS) variables x and Q^2 [1].

However, non-projective crystal geometry faces several limitations when used near the beampipe. The beampipe itself has a complex geometry due to the beam-crossing angle of 25 mrad (35 mrad in detector 2) and includes flanges that link the electron and hadron beampipes. Additionally, the system loads require a support structure near the beampipe with sufficient clearance margins, which further restrict their coverage.

The Yellow Report [1] established an acceptance requirement of $-4 < \eta < 4$. However, it is not feasible to meet the lower limit of this range using only a crystal calorimeter. The current ePIC design positions the crystal ECAL at $z = -174$ cm, with an inner radius of ≈8 cm [2, 3], resulting in a nominal acceptance[1] that reaches $\eta = -3.6$. This limitation is mainly due to the assembly requirements of the ECAL, which necessitate a hole large enough to allow it to slide through the flange further downstream. Figure 1 illustrates that as a consequence, the acceptance coverage near the beampipe is far from optimal. In fact, realistic estimates indicate an acceptance limit of approximately $\eta = -3.5$ [4].

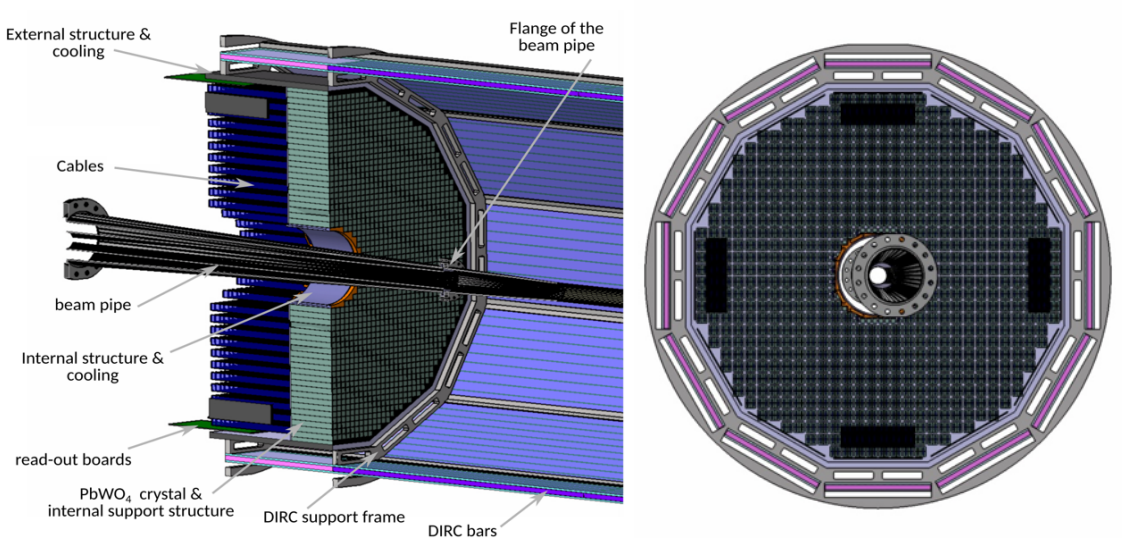

Figure 1: Diagram of the crystal ECAL in the ePIC detector, as of July 2022. Source: Ref. [5]. Note that this is for qualitative reference only.

At the highest EIC energies, $\eta = -3.5$ corresponds to $Q^2 \approx 1$ GeV^2. Consequently, the limited acceptance of the ECAL hinders the study of the transition to the perturbative QCD domain, for which measuring $Q^2 < 1$ GeV^2 is necessary. This limitation affects various physics topics at the EIC, including flagship studies such as searches for gluon saturation.

The very low Q^2 region will be covered by far-backward taggers [1]; however, the transition region $0.1 < Q^2 < 1$ GeV^2 remains beyond the capabilities of existing designs. This issue has recently been discussed within a dedicated "Global-Detector Integration" meeting [4] and the first second-detector workshop [6]. It is referred to as a "Q^2 gap", indicating the missing coverage between the far-backward and central detectors.

[1] Assuming a fiducial selection of showers centered at least 1 cm from the hole.

Some possible approaches have been proposed to bridge the Q^2 gap [7], including lowering the electron beam energy, shifting the interaction point position, and adding dedicated instrumentation between the central detector and the far-backward detectors.

Lowering the electron beam energy, E, helps because the minimum accessible Q^2 scales with E^2. While this is an elegant solution, it comes at the significant cost of reducing the center-of-mass energy of the collisions and, therefore, reducing the coverage at low values of x (the minimum x is proportional to $1/E$). Although this approach may work for some physics topics, it will not allow access to the kinematic region required for gluon-saturation studies.

The second solution of shifting the interaction point was employed at HERA but is completely impractical at the EIC due to the presence of a beam crossing angle, unlike in HERA.

The third solution was implemented at HERA with the ZEUS Beam-Pipe Calorimeter (BPC) and the H1 Very Low Q^2 spectrometer (VLQ). The ZEUS BPC consisted of a tungsten/scintillator calorimeter [8], whereas the H1 VLQ comprised a silicon tracker, a tungsten/scintillator calorimeter, and a time-of-flight system [9]. They reached down to $Q^2 = 0.11$ GeV^2 and $Q^2 = 0.08$ GeV^2, respectively, and helped probe the transition from photoproduction to DIS [10].

The third option is the only viable one and is the focus of our proposal, which aims to develop a detector that will cover a few degrees from the electron-beam direction. We refer to this detector as the Few-Degree Calorimeter (FDC), and will nominally cover $-4.6 < \eta < -3.6$.

Figure 2 illustrates the coverage in the x vs. Q^2 phase-space within the nominal range of the FDC for the top-energy settings for eA (left) and ep (right) collisions. The FDC has the potential to significantly extend acceptance into a key kinematic phase-space and enable the study of the predicted gluon-saturation transition in inclusive DIS [11], as well as many other observables such as exclusive vector-meson production [12, 13].

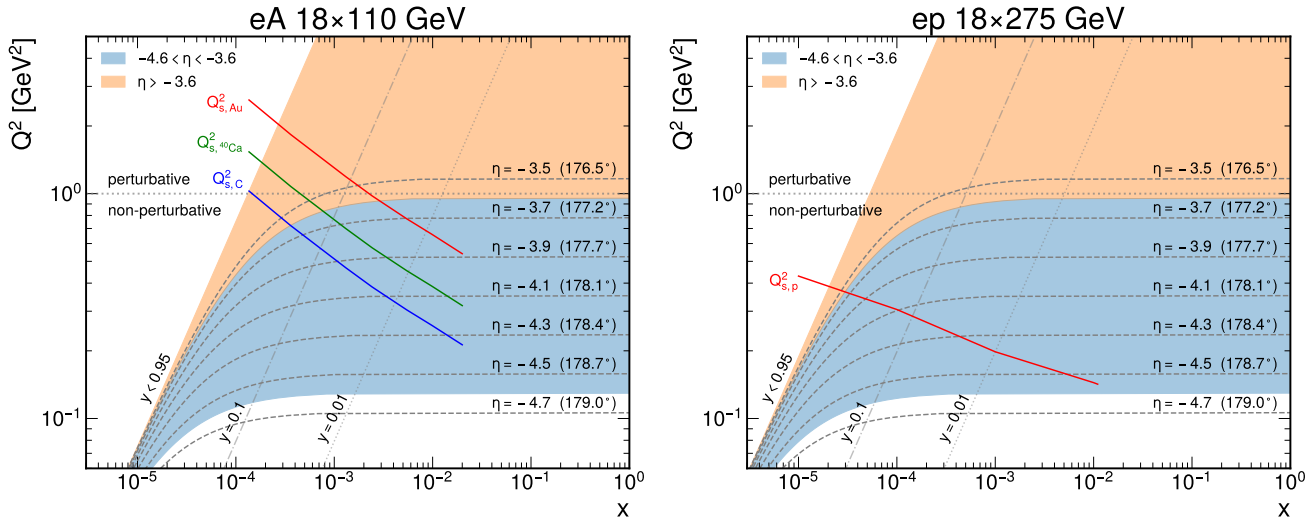

Figure 2: Coverage in the x vs. Q^2 phase-space, with the nominal range of the FDC (blue) spanning $-4.6 < \eta < -3.6$, and the crystal ECAL (orange) spanning $\eta > -3.6$. The left and right panels illustrate the phase-space for top EIC energies for eA scattering and ep scattering, respectively. The colored curves indicate the expected saturation scales, $Q_s(x)$, for various nuclei (left) and the protons (right) [1, 14].

2 Design Constrains and Requirements

2.1 Location and Acceptance

The primary challenge in measuring electron scattering at small angles lies in effectively instrumenting the region near the beampipe while minimizing the material obstructing the detector. It is advantageous to maximize the distance between the interaction point and the detector.

One possibility is to position the FDC behind the crystal ECAL and in front of the backward HCAL, as illustrated in Fig. 3. In the current ePIC design [2], a potential location is at $z = -307$ cm, which would leave space for a compact calorimeter and about 10 cm gap before the HCAL. The overall dimensions of the FDC are determined by the projection of the ECAL hole, along with some additional space for vetoing showers outside the fiducial acceptance.

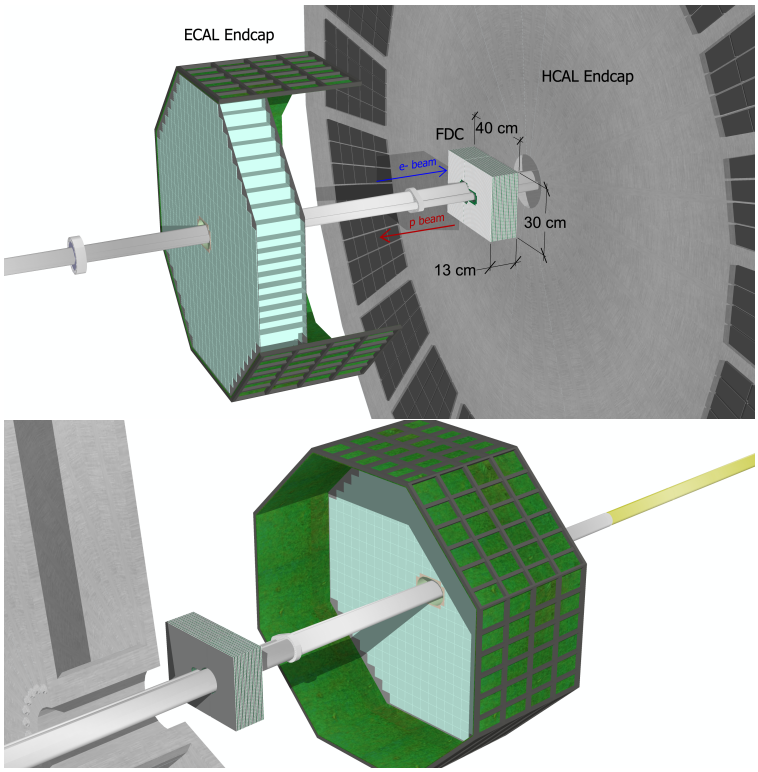

Figure 3: A potential detector layout showcasing the FDC, crystal ECAL, and endcap HCAL. The upper panel provides an upstream view, with the electron beam moving from left to right, while the bottom panel presents a downstream view. The SKETCHUP models for ECAL and HCAL can be found in Ref. [2]. The support structures to the floor are not shown for clarity.

Figure 4 shows that at $z = -307$ cm, the electron beampipe for IP6 has a radius of 4.5 cm, while the hadron beampipe has a radius of 1.8 cm and is shifted 8.3 cm in the x direction. Assuming a 5 mm clearance to the beampipe, similar to the ZEUS BPC [8], a calorimeter with an outer perimeter of 30×40 cm^2 could cover the region $-4.6 < \eta < -3.6$ with non-uniform azimuthal coverage. The shaded region on the FDC represents the area where electrons would encounter part of the ECAL or its support structure before reaching the FDC[2]. This region, which is a few cm wide, would serve as a veto area.

[2]We approximate the path of the electron as a straight line and assume that the flat cables servicing the crystal calorimeter SiPMs can be arranged to avoid the hole area.

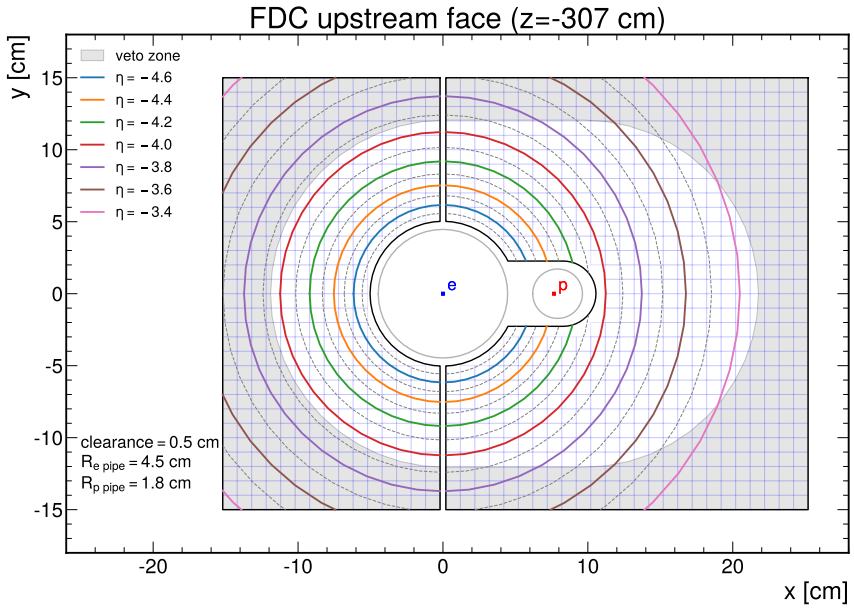

Figure 4: Transverse view of the FDC, assuming a location at $z = -307$ cm, with rings of constant η superimposed. The electron and hadron beampipes are represented by their transverse cut, along with a 10×10 mm^2 grid for reference. The non-shaded area is a projection from the ECAL hole.

Figure 5 shows projections of the possible detector layout, including both the yz and xz views. The ECAL hole is currently assumed to have a height of 14.7 cm and a width of 20.5 cm, taking into account the current version of the "micro-flange" (with a cam shape that is 15.2 cm wide and 11.1 cm tall) and a required clearance of 1.8 cm, 3.6 cm, 1.8 cm, and 1.7 cm between the flange and the ECAL's inner support structure on the top, right, bottom, and left sides when looking downstream [3]. This specific reference is provided to highlight the FDC potential in ePIC. However, it is important to note that the layout of detector 2 may offer additional optimization possibilities, which we intend to explore further.

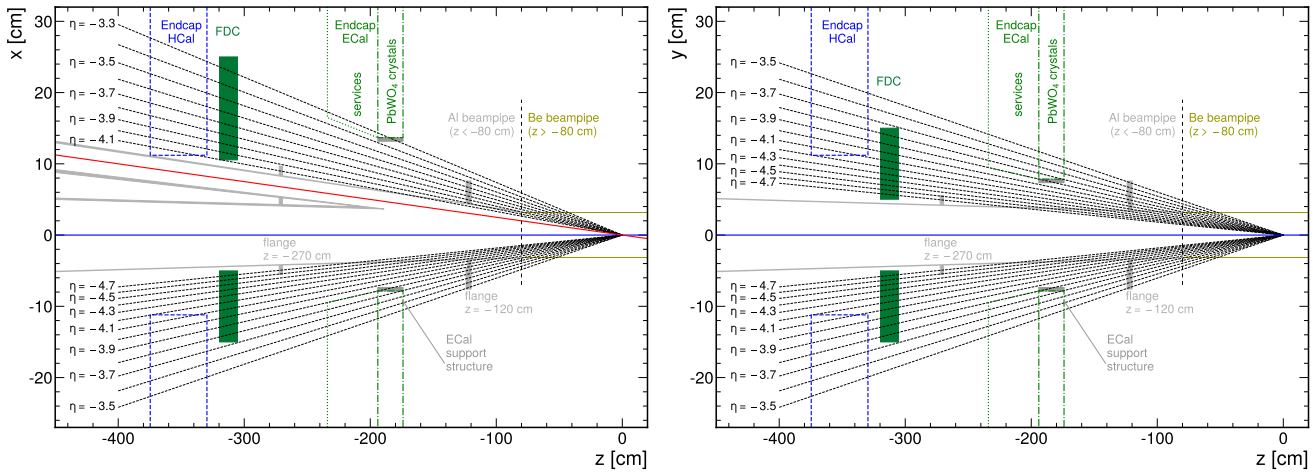

Figure 5: A potential location for the FDC is behind the backward ECAL in the current ePIC design. This diagram illustrates the dimensions and locations of ECAL and HCAL as per Ref. [2]; the flanges and clearance dimensions as per Ref. [3], and ECAL support structure as per Ref. [15].

2.2 Dead Material in Front of FDC and Mitigation Strategy

The main challenge faced by a detector located in a high pseudorapidity range is that particles can encounter a significant amount of material as they graze the beampipe walls. While converted electrons and photons can be identified through shower-shape information, reducing the amount of material helps improving efficiency and minimizing background.

Figure 6 illustrates the number of radiation lengths of beampipe material encountered by electrons before reaching the FDC, as a function of η. Within most of the FDC acceptance, the total number of radiation lengths ranges from 0.5 to 1.2 and reaches a maximum of 1.8 at $\eta = -4.7$. Approximately half a radiation length is contributed by the flange at $z = -120$ cm within the range of $-4.2 < \eta < -3.5$. The significant increase in the total number of X_0 traversed at around $\eta = -4.0$ is attributed to the use of aluminum instead of beryllium in the beampipe for $z < -80$ cm.

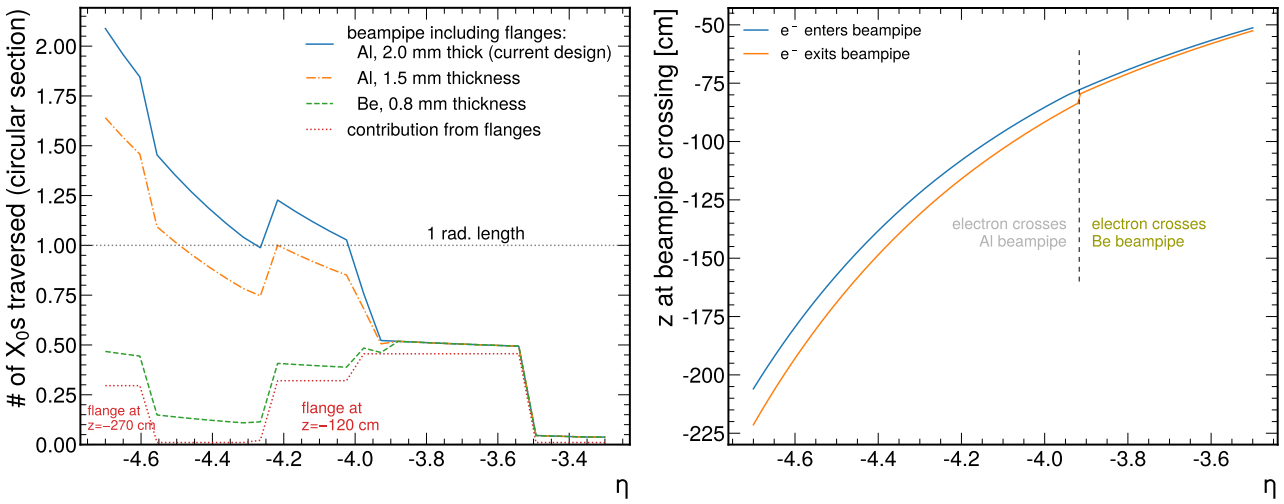

Figure 6: Left: The beampipe material encountered by electrons before reaching the FDC. It includes the IP6 beampipe model (solid blue), a modified version with a thinner aluminum (red dashed), and another scenario with beryllium (green dot-dashed). The contribution from the flanges is represented by the red dotted curve. Right: The position of the scattered electron's encounter with the beampipe as a function of η.

The HERA experiments successfully addressed this challenge by implementing a beampipe "exit window" made of thin aluminum, which reduced the total dead material to less than 1 X_0 [9]. Alternatively, one could use a beryllium section. To estimate the required location and length of the exit window for the FDC, we calculated the point of the electron's impact on the beampipe a function of η, which is shown in the right panel of Fig. 6. In this calculation, we made the assumption that the electron travels in a straight line from the nominal interaction point.

A beryllium section within the range of $-205 < z < -80$ cm would significantly reduce the total material budget in the $-4.7 < \eta < -4.1$ region to less than 0.5 X_0, as shown in the left panel of Fig. 6. Alternatively, using 1.5 mm aluminum would result in a reduction to less than 1 X_0 for $\eta > -4.5$.

Another effective method for mitigating the impact of dead material is use shower shapes to tag converted electrons or photons that originated further upstream in the beampipe or flanges [8]. Such showers will have broader transverse dimensions and atypical longitudinal development. This emphasizes the need for fine granularity in both the transverse and longitudinal directions.

2.3 Absorber Material Considerations

To enable accurate FDC measurements at large η, it is crucial to minimize energy leakage into the beampipe. Figure 7 shows the distance to the beampipe as a function of η. The target value of $\eta = -4.6$ corresponds to about 18 mm from the electron beampipe at $z = -307$ cm. Assuming a 5 mm clearance, this leaves 13 mm between the edge of the detector and $\eta = -4.6$. For reference, the ZEUS BPC measured 95% of the energy from 5 GeV electrons at 8 mm from the detector's edge in test beams [8]. The ZEUS BPC had a 13 mm Moliere radius, so based on scaling, we can assume that the FDC needs an effective Moliere radius less than 21 mm to measure electron showers at $\eta = -4.6$ with 95% coverage.

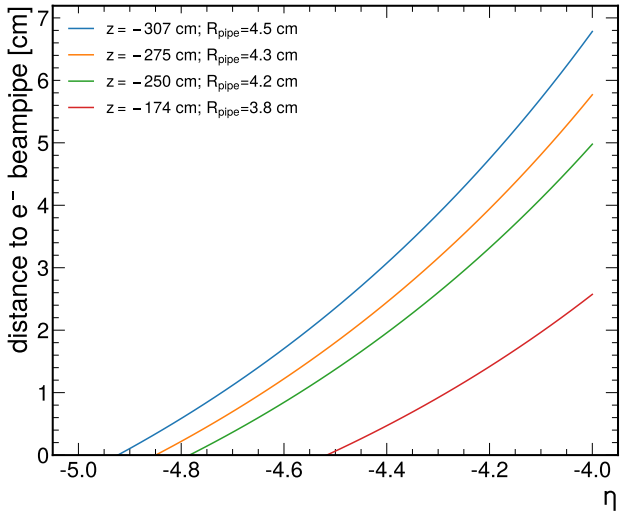

Figure 7: Distance from the electron beampipe as a function of η at various z locations, including the proposed FDC position (blue) and the location of the ECAL endcap (red).

Another factor influencing the selection of the FDC absorber is the background originating from hadronic showers (as quantified in Section 2.5). To mitigate this, it is beneficial for the FDC to have a small ratio of nuclear interaction lengths to radiation lengths. Table 1 presents characteristics of potential materials for the FDC. The probability of hadron interactions can be minimized by using tungsten (by about 20% compared to lead-tungsten and by a factor of 55% compared to iron).

Table 1: Equivalent number of nuclear interaction lengths for a depth of 20 X_0 and the probability of hadron interaction ($1 - e^{-\lambda}$).

	X_0	λ	20 X_0 equivalent	$1 - e^{-\lambda}$
W	0.35 cm	9.94 cm	0.7 λ	0.50
Fe	1.76 cm	16.77 cm	2.1 λ	0.88
$PbW0_4$	0.89 cm	20.27 cm	0.9 λ	0.60

2.4 Energy Range

The main objective of the FDC is to identify and measure the energy and angle of electrons in the $0.1 < Q^2 < 1.0$ GeV^2 range. Figure 8 illustrates the minimum electron energy as a function of η for various Q^2 values. The minimum energy required for $-4.6 < \eta < -3.6$ falls within the range of 2–13 GeV, whereas the maximum is the beam energy. Thus, the target energy range is 2–18 GeV.

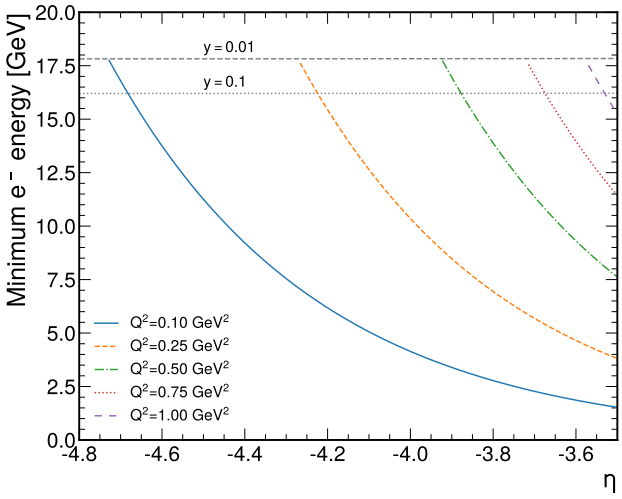

Figure 8: Minimum energy of electrons for a given Q^2 as a function of η.

2.5 Background Rejection

The main background for inclusive DIS measurements originates from events with small Q^2, where the scattered electron is not detected, but an electron candidate is observed in the FDC. Figure 9 shows the expected particle spectra obtained using PYTHIA6 to simulate ep scattering without a Q^2 cut and without considering detector effects. In the absence of charge tagging, both electrons and positrons from semi-leptonic decays contribute to the background. Similarly, the charged-pion background includes both charges. The photon background primarily arises from neutral-pion decays.

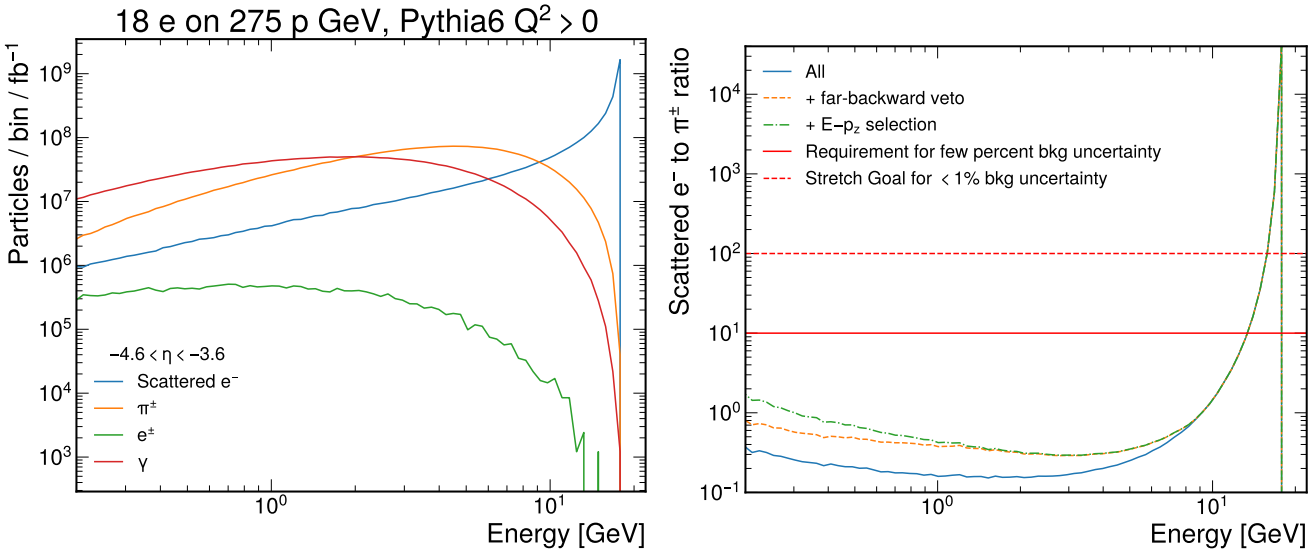

Figure 9: Left: Particle spectra per fb^{-1} of integrated luminosity, estimated using PYTHIA6 with no Q^2 cut. Right: Ratio of scattered electrons to charged pions as a function of energy.

We estimate the background rejection power of approaches employed at HERA [10, 8] and the EIC YR. Specifically, we use the far-backward detectors as a veto for photoproduction and select events based

on their energy-momentum imbalance[3] with a loose selection of $E - p_z > 18$ GeV [1].

The right panel of Fig. 9 illustrates the impact of these cuts on the e/π ratio. The far-backward veto has a modest effect due to its small acceptance [1]. Similarly, the $E - p_z$ cut has a modest impact, since for background events the scattered electron has low energy. Overall, the resulting e/π ratio is about $e/\pi \approx 0.4$ between 1–6 GeV, $e/\pi \approx 1$ around 10 GeV, and increases rapidly at higher energies. Similarly, the resulting e/γ ratio ranges from 0.1 to 1 for $E < 6$ GeV and increases at higher energies. The background of positrons and electrons from semi-leptonic decays reaches 10% at 1 GeV, decreasing to less than 1% at 10 GeV. Since there is no magnetic field near the FDC, this background cannot be subtracted using reverse field runs. Instead, Monte Carlo studies would be employed to estimate and subtract it. Alternatively, electron-isolation criteria might reduce this background further.

The FDC measurements should yield a purity greater than 90% in order to achieve background uncertainties at the few percent level [1]. A purity of 99% would yield a negligible uncertainty relative to the expected luminosity uncertainty of 1%. We set the former as a requirement and the latter as a stretch goal. Therefore, the required rejection power falls within the range of 10–25 for $\pi^{\pm}$ and 10–100 for γ, with a factor of 10 higher for the stretch goal.

The standalone FDC's $\pi^{\pm}$rejection power will rely on its shower-shape capabilities. Longitudinal segmentation can play a crucial role in discriminating hadrons, as they are more likely to interact deeper within the detector, while electrons tend to exhibit showers starting primarily in the initial layers. Moreover, transverse segmentation is also necessary, as electrons typically produce narrower and more regular showers compared to hadronic ones. This approach is expected to work well above a few GeV.

Additional background rejection can be achieved through auxiliary systems, such as a scintillator layer for tagging MIPs to reject unconverted photons, or a TOF system to reject low-energy hadrons. The background from unconverted photons can be effectively reduced with a scintillator that has an efficiency greater than 99%. Figure 10 demonstrates the potential of TOF and illustrates that a time resolution of about 50 ps would be necessary to achieve a 2σ e/π separation below 1 GeV.

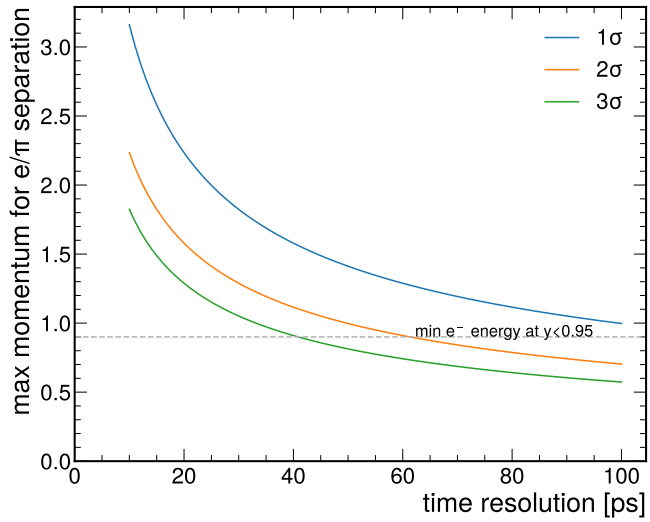

Figure 10: Required time resolution to discriminate between electrons and charged pions using TOF as a function of the particle's momentum. These requirements are based on a location at $z = -307$ cm.

[3]The $E - p_z$ distribution peaks at twice the electron-beam energy when the scattered electron is correctly identified.

2.6 Summary of Requirements

The FDC calorimeter technology needs to meet the following requirements:

- Maximize the acceptance near the beampipe by using an absorber with small Molière radius to mitigate energy leakage and by employing a self-supporting structure.
- Provide high granularity in both the transverse and longitudinal directions to enhance rejection capabilities for backgrounds such as charged pions, converted photons/electrons, and beam-gas interactions.
- Provide position and energy resolution for electrons in the range of 2–18 GeV that is sufficient for conducting cross-section measurements with 5 bins per decade in both Q^2 and x.
- Offer excellent time resolution to identify beam-induced and low-energy hadron backgrounds.

These are quantified in Table 2. The energy and position resolutions follow the ZEUS BPC design [8].

Table 2: Summary of physics-inspired requirements for FDC

Requirement	Value/Range	Justification
η range	$\eta_{\min} = -4.6$	Get to $Q^2 \approx 0.1$ GeV^2 limit
ϕ range	$0 < \phi < 2\pi$	Maximize acceptance
Energy range	2–18 GeV	Follows from kinematics for $Q^2 > 0.1$ GeV^2
$\pi^{\pm}$ rejection	$> \times 25$ at 90% eff. in 1–10 GeV	Purity for F_2 measurement with 90% purity
γ rejection	$> \times 100$ at 90% eff. in 1–10 GeV.	Purity for F_2 measurement with 90% purity
Moliere radius	< 21 mm	$> 95\%$ shower containment at $\eta = -4.6$
Energy resolution	$< 17\%/\sqrt{E}$	Sufficient x, Q^2 reconstruction
Position resolution	< 2 mm$/\sqrt{E}$	Sufficient x, Q^2 reconstruction
Time resolution	< 50 ps	Rejection of $\pi^{\pm}$ below $\approx$1 GeV

3 Design

3.1 HERA Precedent and State-of-the-Art

Our design draws inspiration from the ZEUS BPC [8] and H1 VLQ [9] calorimeters, incorporating modern enhancements in optical readout and photosensors. It leverages recent advancements in high-granularity calorimetry [16], led by the CALICE collaboration, as well as improvements in SiPM technology [17]. These developments offer the potential for substantial improvements in granularity at a reasonable cost for a small detector such as the FDC.

The CALICE collaboration has tested a scintillator-tungsten ECAL with WLS fiber readout coupled to SiPMs [18, 19]. The tested strips had widths of 10 or 5 mm. By applying a "split-strip algorithm" [20], this prototype achieved an effective granularity close to 10×10 mm^2 or 5×5 mm^2. The test-beam data resulted in an energy resolution of $12\%/\sqrt{E} \oplus 1.2\%$. More recently, this design has been superseded by a "SiPM-on-tile" approach, where the SiPM is air-coupled to the scintillator strip. The Chinese Electron-Positron Collider (CEPC) and CALICE collaborations have built a 6.7k channel SiPM-on-tile prototype, which is undergoing testing at CERN in 2023 [21].

Table 4 summarizes our target design in comparison with the ZEUS, H1, CALICE and CEPC designs.

Table 3: Summary description of our proposed EIC FDC, the ZEUS BPC [8], the H1 VLQ [9], the CALICE ScECAL [18, 19], and the CEPC ScECAL [22, 23, 24]. The number of channels for CALICE/CEPC refer to the latest prototypes.

	EIC FDC	ZEUS BPC	H1 VLQ	CALICE	CEPC
Test beam	2024 planned	1994	1997	2009	2023
Depth	20 X_0	24 X_0	16.7 X_0	21.5 X_0	22 X_0
W/Sc thickness	3.5/2 mm	3.5/2.6 mm	2.5/3 mm	3.5/3 mm	3.5/2 mm
Moliere Radius	15 mm[4]	13 mm	15 mm	20 mm	20 mm
Optical readout	SiPM-on-tile	WLS bar+PMT	WLS bar+PIN	WLS fiber+SiPM	SiPM-on-tile
Trans. granularity	10×50 mm^2	7.9×150 mm^2	5×120 mm^2	10×45 mm^2	5×45 mm^2
Long. granularity	every strip	none	none	every strip	every strip
Readout channels	4500	31	336	2160	6720
Electronic readout	HGROC	FADC/TDC	ASIC	SPIROC	SPIROC2E
Position resolution	3.6 mm/$\sqrt{E}$	2.2 mm/$\sqrt{E}$	2 mm/$\sqrt{E}$	—	—
Energy resolution	$\frac{17\%}{\sqrt{E}} \oplus 2\%$	$\frac{17\%}{\sqrt{E}} \oplus 2\%$	$\frac{13\%}{\sqrt{E}} \oplus 3\%$	$\frac{12.5\%}{\sqrt{E}} \oplus 1.2\%$	$\frac{15\%}{\sqrt{E}} \oplus 1\%$
Time resolution	<50 ps	400 ps	—	—	—

3.2 Proposed Design

Figure 11 shows the FDC design which includes alternating layers of vertical and horizontal scintillators that are wrapped in reflective foil and read out using SiPMs (HPK 14160-1315PS). The scintillator strips measure 50 × 10 × 2 mm (length, width, thickness) and feature a dimple at the center for air-coupling with the SiPM. Each tungsten layer is 3.5 mm (1 X_0, and 0.035λ). The total FDC consists of 20 layers,

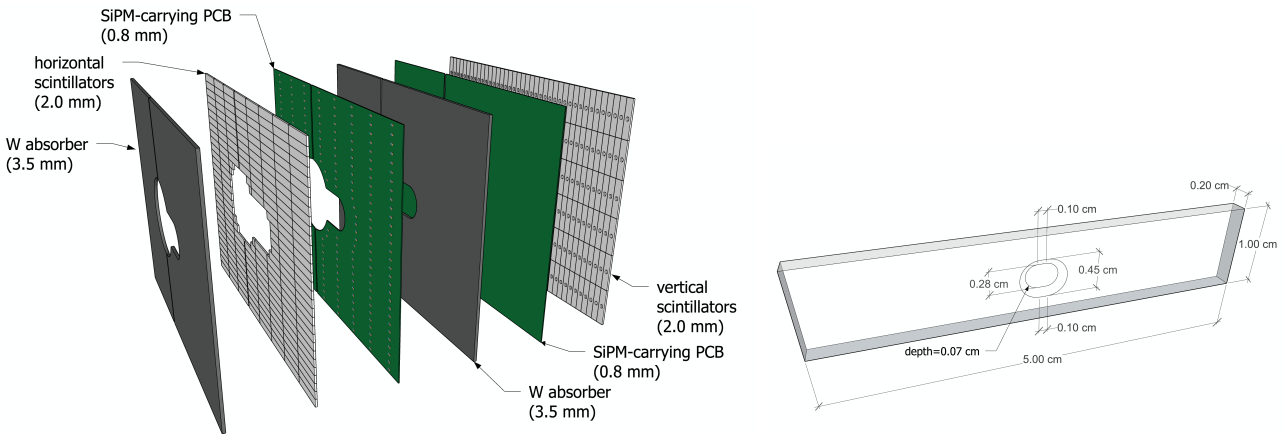

Figure 11: Left: exploded view of a double layer of the FDC. Right: dimensions of a single scintillator.

for a total of 20 X_0. Figure 12 shows the FDC dimensions, including the hole for the beampipes assuming a clearance of 5 mm. The detector is divided into two parts, allowing one half to be retracted to the left and the other half to the right for maintenance purposes. The FDC material as function of η and ϕ is shown in the right panel of Fig. 12. Up to about $\eta = -4.1$, the detector has full coverage in ϕ, whereas at larger negative η, the hole for the hadronic beampipe removes up to 60° of acceptance.

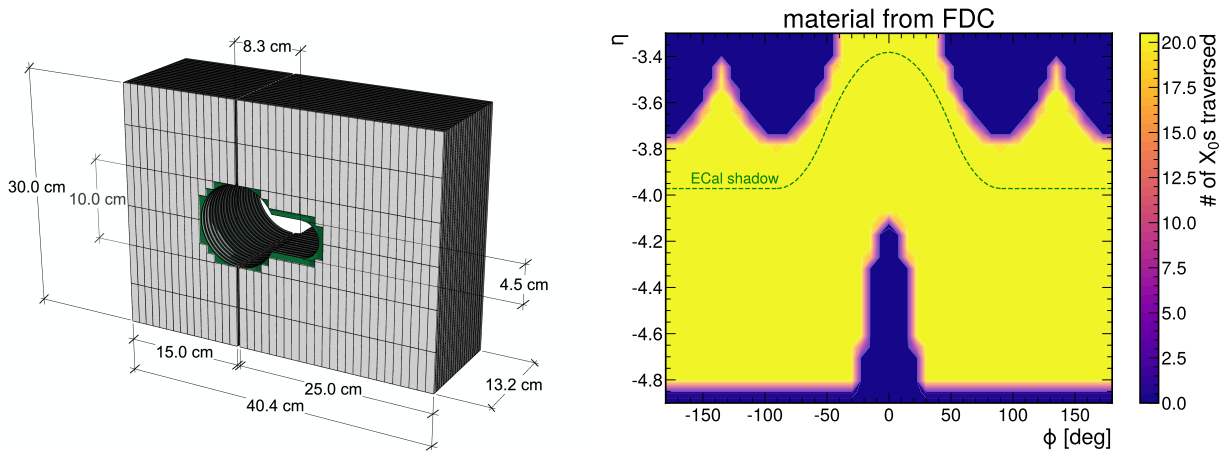

Figure 12: Left: Dimensions of the FDC. Right: FDC material as a function of η and ϕ. The dashed curve represents the boundary of the fiducial region of the FDC.

3.3 Simulation

We used the DD4HEP framework to simulate electrons generated with a uniform azimuthal angle at various η points in order to estimate the FDC performance. Currently, the simulation does not include any dead material. However, as part of the proposed project, we plan to include the beampipe material and develop background rejection algorithms.

3.3.1 Energy Resolution

Figure 13 shows the energy resolution, which can be parameterized as $17\%/\sqrt{E} \oplus 2\%$, and is consistent with the ZEUS BPC data [8]. We also compare it to CALICE data, which exhibits improved performance at the expense of a larger Moliere radius. The right panel of Figure 13 displays the energy resolution and scale as a function of η. The performance remains relatively stable for $\eta > -4.6$.

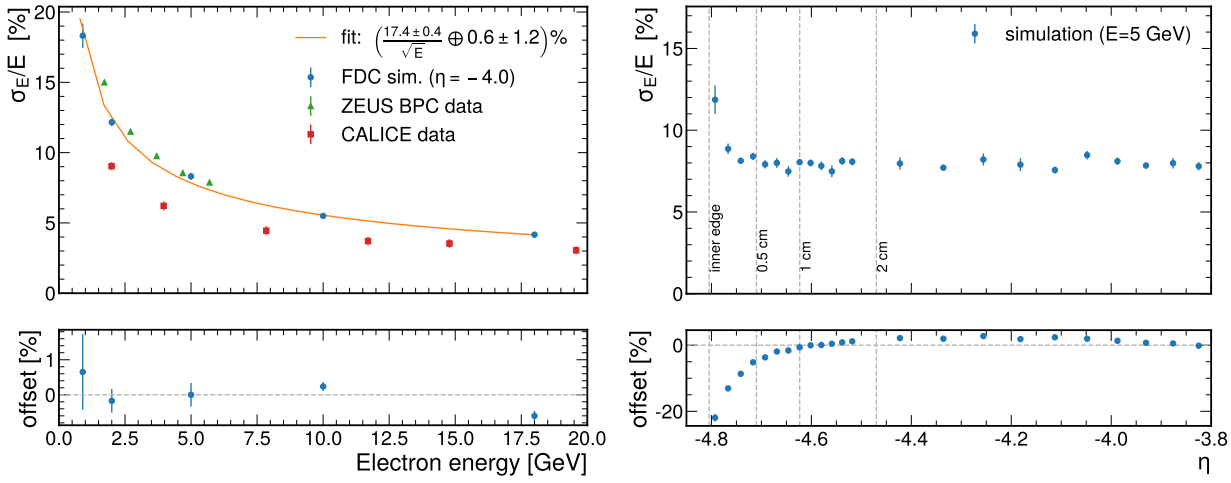

Figure 13: Left: FDC energy resolution at $\eta = -4.0$ compared to ZEUS BPC [8] (green triangles) and CALICE [20] (red squares) data. Right: Dependence of the energy resolution on η. Vertical lines indicate different distances from the edge of the hole.

3.3.2 Position Resolution

The polar angle resolution is determined by considering the position resolution of the FDC, denoted as δR, and the resolution of the vertex position, denoted as δz_0. In the small-angle approximation:

$$\delta\theta \approx \frac{\delta R \oplus (\pi - \theta)\delta z_0}{z} \tag{1}$$

The electron vertex position can be precisely determined by tracking other particles in the event using the main detectors, as was done in HERA [8, 9]. Thus, only the FDC position resolution is relevant.

We reconstructed the x and y values following the method described in Ref. [25]:

$$x = \frac{\sum\limits_{i \in v\,layers} w_{X,i} x_i}{\sum\limits_{i \in v\,layers} w_X} \quad \text{and} \quad y = \frac{\sum\limits_{i \in h\,layers} w_{Y,i} y_i}{\sum\limits_{i \in h\,layers} w_Y} \tag{2}$$

where the weights $w_{X,i}$ and $w_{Y,i}$ are determined by

$$w_{X,i} = \max\left(0, w_0 + \log\frac{E_i}{\sum_{j \in \text{v layers}} E_j}\right) \quad \text{and} \quad w_{Y,i} = \max\left(0, w_0 + \log\frac{E_i}{\sum_{j \in \text{h layers}} E_j}\right) \tag{3}$$

The "h layers" sums are over layers with horizontally aligned strips and the "v layers" sums are over layers with vertically aligned strips. The cutoff parameter w_0 is set to 4.0.

Figure 14 shows the position resolution as a function of energy. For energies greater than 1 GeV, the position resolution is better than the strip width divided by $\sqrt{12}$. The resolution we obtained is poorer than the ZEUS BPC resolution. This difference can be partially explained by the smaller strip width (7.9 mm vs 10 mm), but it may also include components from algorithm tuning, which we will further explore and optimize.

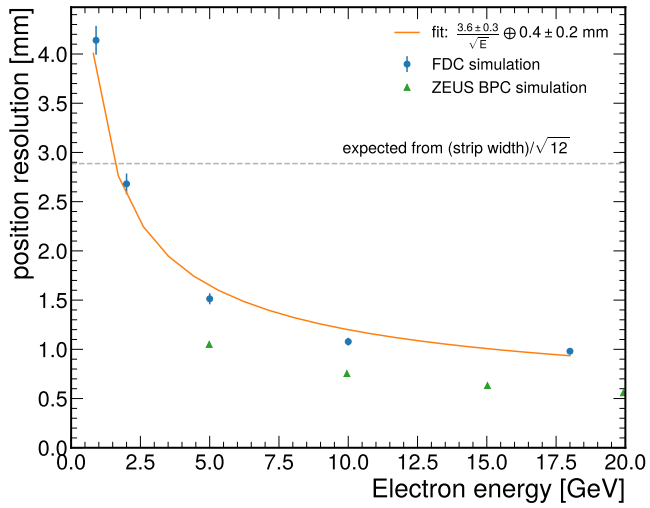

Figure 14: Position resolution of the FDC detector. This is compared to the resolution determined via simulations for the ZEUS BPC [8] (green triangles)

3.3.3 Kinematic Variable Reconstruction

The resolution in Bjorken x and Q^2 can be derived from those of the electron energy $\delta E'_e$ and of the electron polar angle $\delta\theta_e$ (using the small-angle approximation):

$$\frac{\delta Q^2}{Q^2} \approx \frac{\delta E'_e}{E'_e} \oplus \frac{2}{\pi - \theta_e}\delta\theta_e, \qquad \frac{\delta x}{x} \approx \frac{1}{y}\frac{\delta E'_e}{E'_e} \oplus \left(\frac{x}{E_e/E_p} - 1\right)\frac{2}{\pi - \theta_e}\delta\theta_e \tag{4}$$

In the non-divergent region (*i.e.* $y > 0.1$), the Q^2 resolution ranges from 4% to 14% depending on kinematics, whereas the x resolution ranges from 10% to 50% with a strong y dependence.[5]

To quantify these resolutions in the context of inclusive DIS measurements, we followed the EIC YR approach and calculated the corresponding purity and stability values. In this context, purity is determined by calculating the fraction of events reconstructed in a specific bin that were also generated in that bin (i.e., $P = N_{(\mathrm{rec,gen})}/N_{\mathrm{rec}}$). Stability is calculated as the fraction of events generated in a specific bin that were also reconstructed in that bin (i.e., $S = N_{(\mathrm{rec,gen})}/N_{\mathrm{gen}}$). Here, $N_{(\mathrm{rec,gen})}$ represents the number of events where the electron is both generated and reconstructed in the same bin. For the generated events, we used the same Pythia6 simulation as described in Section 2.5.

Figure 15 shows the resulting purity and stability plot for events with $-4.6 < \eta < -3.6$. The plot has 5 bins per decade in both x and Q^2, similar to the EIC YR studies [1]. Purity and stability values above 50% are observed for the phase-space covered with $y > 0.1$, with some degradation at lower values, as expected when using the electron reconstruction method exclusively. It is anticipated that the performance for $0.01 < y < 0.1$ will improve by combining the electron and hadronic methods.

Overall, these studies demonstrate that the FDC design can provide sufficient resolution for measuring kinematic variables in the low x, low Q^2 region, thereby bridging the Q^2 gap.

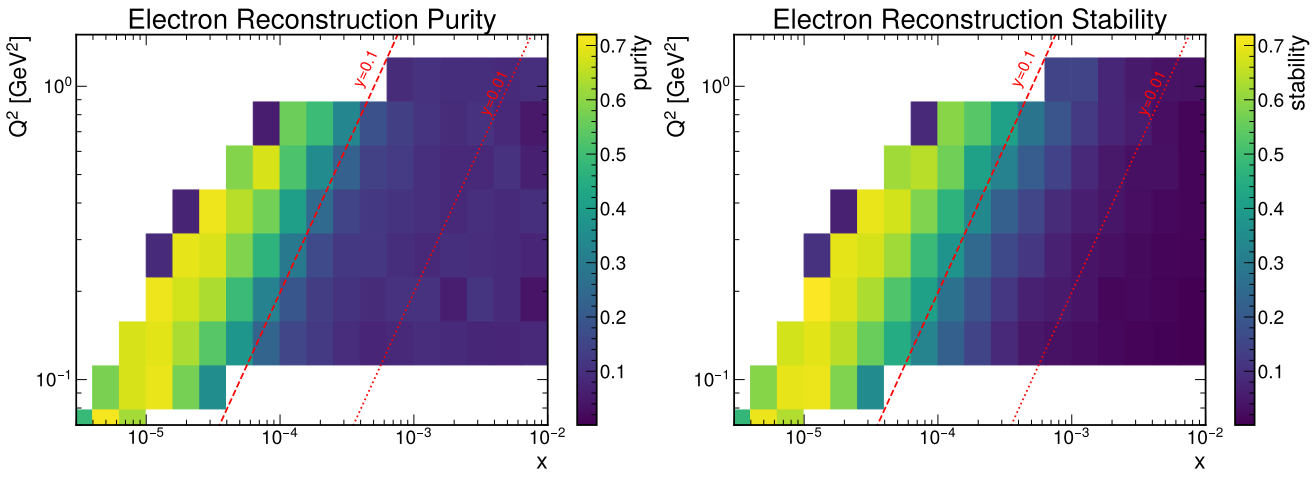

Figure 15: Purity (left) and Stability (right) for reconstruction of x and Q^2 using the FDC and the electron method.

[5] As detailed in the 2021 EIC Conceptual Design Report (CDR) [26], the electron beam 1-sigma angular divergence can be as large as 200 μrad. The will affect the kinematic reconstruction for electrons scattered at angles less than 10 mrad. Since the FDC acceptance begins at 20 mrad, the reconstruction of the inclusive kinematic variables will not be degraded by beam-divergence effects.

3.3.4 Shower-shape Examples

Figure 16 shows 3D and projection views of example showers. The three scenarios depicted are: an electron reaching the FDC with no material in front of it (left), a photon that initiated showering in the beampipe (middle), and a π^-. Among the three cases, the electron without pre-showering produces the narrowest shower, while the pre-showering photon and the π^- generate more irregular showers.

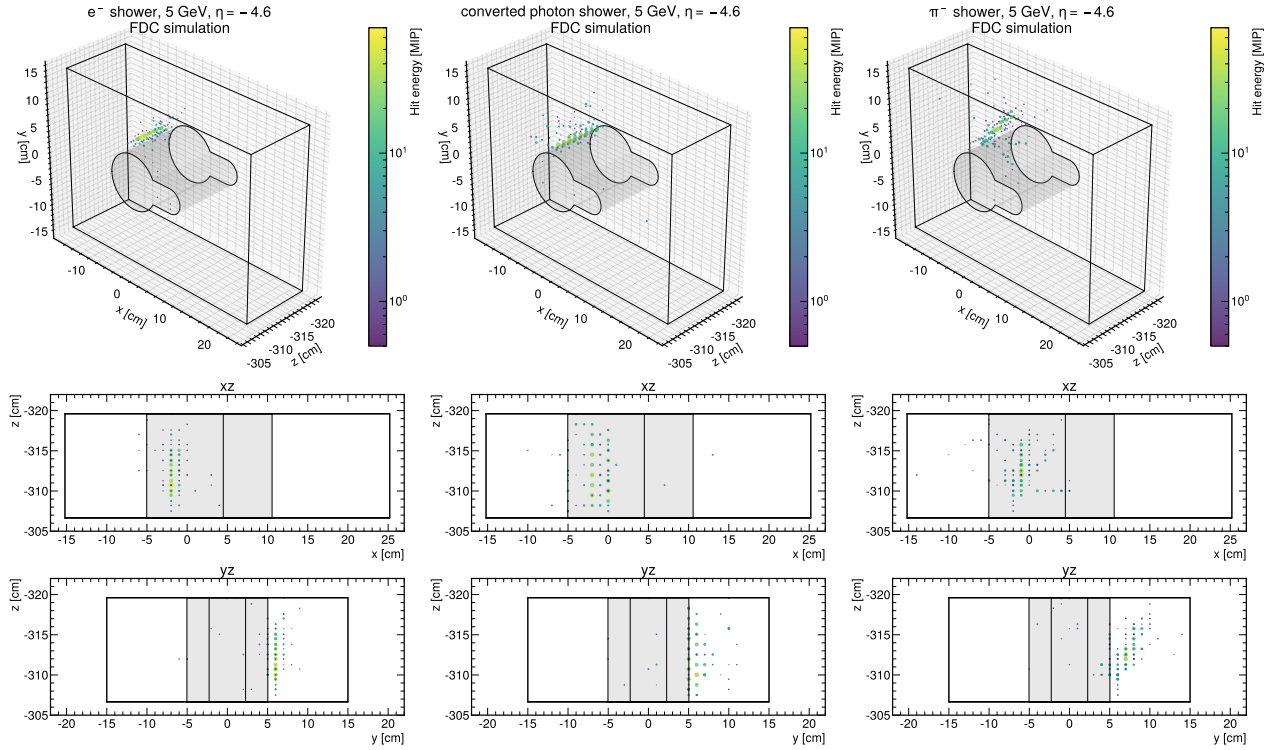

Figure 16: Examples of reconstructed showers are shown for electron (left), converted-photon (middle), and charged pion (right), with 5 GeV and $\eta = -4.6$. The displayed granularity is 10×10 mm^2, which represents the expected effective granularity of the FDC after applying the strip-split algorithm [20]. The color code and marker size represent the hit energy.

This illustrates the potential of 5D shower shape analysis to reject background. We will assess this potential through comprehensive simulations of converted electrons/photons, hadron showers, and beam-gas background. In terms of converted-electron tagging, the showers are expected to exhibit broader transverse profiles and anomalous longitudinal development. For hadron tagging, the fine segmentation will be primarily used to identify the starting point of the shower, which is more likely to be located at a deeper position compared to electrons. Moreover, the hadron showers will also have a different time development, with hits at later times compared to electron showers.

4 Research Plan

We have devised a research plan that will involve test-bench measurements and simulation studies to showcase the potential of high-granularity calorimetry for background rejection. This plan will culminate in the development of a prototype that will undergo testing at JLab. The following sections outline our objectives, while Section 4.4 details the corresponding deliverables and milestones.

4.1 Test-Bench Measurements and Timing Studies

We aim to develop the design of the FDC by establishing a set of baseline measurements for its building blocks, specifically the scintillator strips readout with SiPMs. These measurements will characterize light yield, uniformity, and time resolution. We will build upon our recent studies that resulted in a JINST paper [27], which focused on similar measurements for the ePIC Calorimeter Insert [28].

Our main emphasis will be on timing studies, as this area is experiencing rapid development. Notably, preliminary studies have been conducted by CALICE in this field [29], and the CEPC collaboration is designing a timing layer [30]. In particular, we will investigate a cell design for a timing layer, which may involve a specialized strip geometry and/or a larger SiPM model to enhance light yield, as time resolution is driven by photostatistics.

To conduct these measurements, we will use our existing test-bench setup at UCR, which includes a picosecond laser (Hamamatsu PLP-10, 440 nm) and a 5 GHz full-waveform digitizer (DRS4 board). By the end of this study, our goal is to establish a potential SiPM-on-tile timing layer that could be incorporated into the FDC, either at the location of the shower maximum or as a pre-shower. This approach could achieve a per-strip resolution of 50 ps and shower resolution of O(10) ps through the combination of multiple strips, which is also the current aim of CEPC/CALICE [30]. Alternatively, we will investigate a pre-shower with LYSO and SiPMs, which would enable a resolution of 30 ps [31].

4.2 The First FDC Prototype

We have planned to construct an FDC prototype and conduct testing at JLab in FY24. Figure 17 illustrates its dimensions, which are 10×10 cm^2 with a length of approximately 39 cm. The prototype will comprise 16 layers, each containing 20 scintillator strips arranged in either a horizontal or vertical orientation. With a total of 320 channels, this prototype will represent approximately 7% of the total number of channels envisioned for the final FDC design.

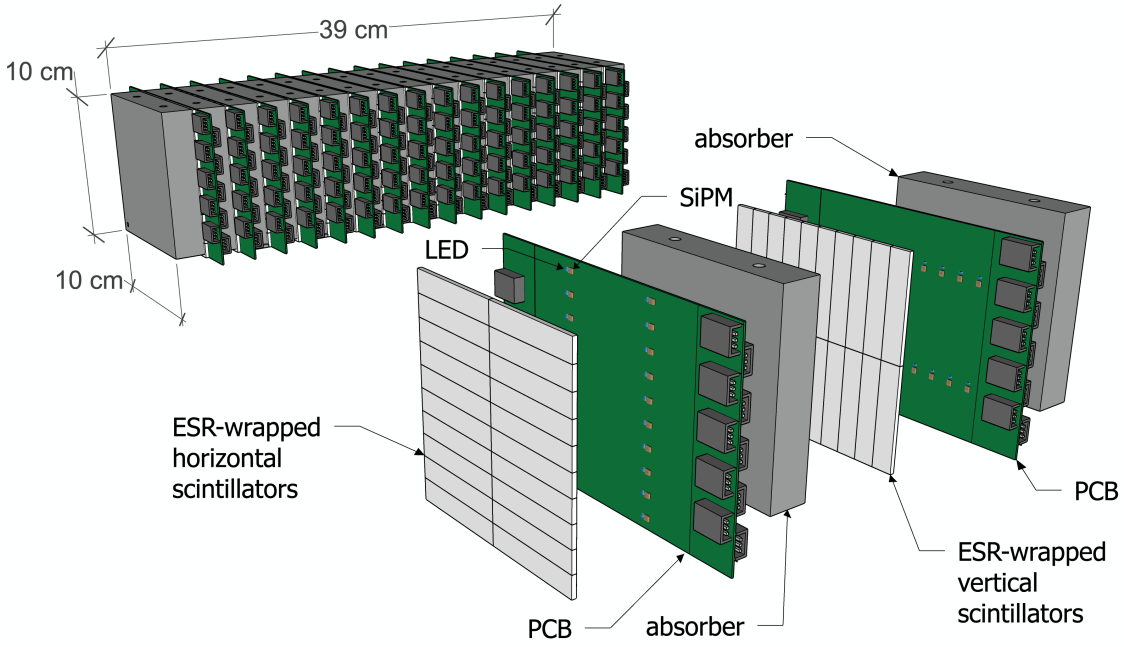

Figure 17: Exploded view of planned FDC prototype.

The steel blocks have dimensions of approximately $10 \times 10 \times 2$ cm^3 (shown in left panel of Fig. 18). Each block has a thickness of $1.1X_0$, comparable to the proposed FDC design that uses 3.5 mm tungsten. Future iterations of this prototype will use tungsten plates.

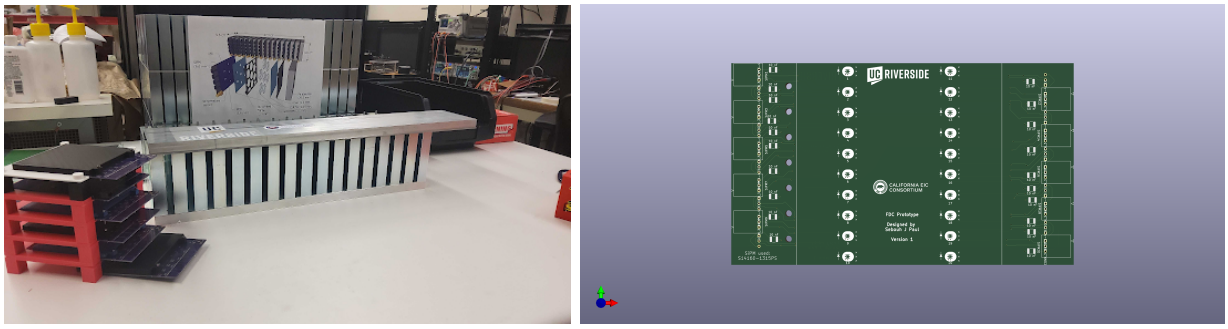

Figure 18: Left: Steel block structure intended for use in the FDC prototype. Right: SiPM-carrying boards designed for the FDC prototype.

The SiPM board, which accommodates twenty 14160-1315PS units, will have a thickness of 0.8 mm and will include UV LEDs. Our current design for this board is shown in the right panel of Fig. 18. The SiPM board will be connected to the CAEN FERS-5200 unit using coaxial cables and custom connectors. The CAEN FERS-5200 unit houses 2 CITIROC 1A ASIC chips and can independently bias and readout a total of 64 SiPMs. Groups of UV LEDs will be connected in series and will be linked to a pulse generator via a BNC connector.

We plan to fabricate small strips from EJ-212 scintillator sheets. Our group has extensive experience in this field and has successfully produced numerous small hexagonal cells with a dimple, as illustrated in Figure 19. We will use the same approach to make scintillator strips.

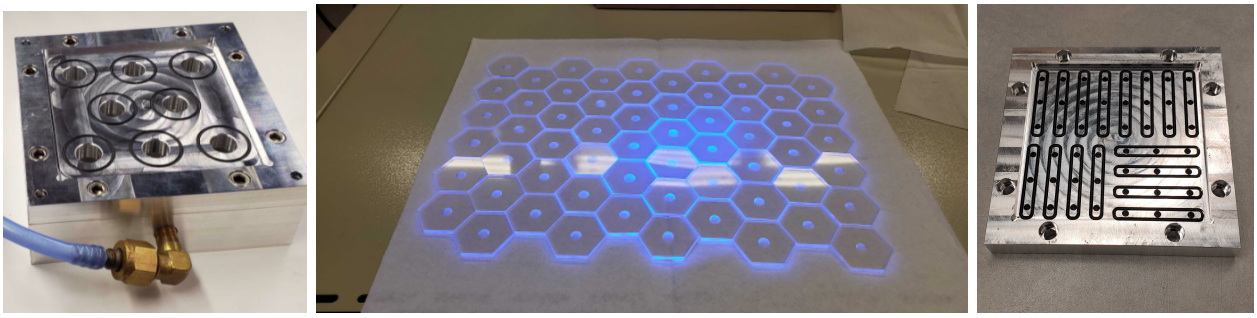

Figure 19: Left: Vacuum chuck used to machine EJ-212 scintillator sheets into cells with dimple geometry (with hexagonal shape, for the calorimeter insert). Middle: example of machined cells. Right: Vacuum chuck designed for machining FDC strips.

Table 4 presents the estimated cost for the materials required for our planned FDC prototype.

We are planning to conduct a test beam in Hall-D in FY24. The objectives of this test beam are to advance the FDC design, validate its simulations, and demonstrate the production capabilities, operation, and calibration of the SiPM-on-tile design. We aim to showcase channel-by-channel calibration with MIPs and monitor the gain using UV LED. Note that our team recently conducted a successful test beam for the ePIC Calorimeter Insert in January 2023.

Table 4: Estimated Cost of the FDC Prototype. The quantities of SiPMs and scintillators include spare units.

Material	Description	Units	Cost per unit	Total cost	Info
Scintillator	EJ-212 $10 \times 10 \times 0.2$ cm	40	\$80	\$3.2k	Recent quote
SiPMs	S14160-1315PS	500	\$22	\$11k	Recent quote
ESR foil	26×26 in sheet	2	\$2k	\$4k	Recent quote
PCBs	0.8 mm from OSH-Park	20	\$80	\$1.6k	Recent quote
Bias and readout	CAEN FERS-5200	5	\$8k	\$40k	Recent quote
Supplies	Glue, wipes, gloves, etc	—	—	\$3k	Educated guess
Fe blocks	$10\times10\times$ 3 cm^2	—	—	in kind	–
Machining	UCR machine shop	100 hr	\$36	\$3.6k	Educated guess
Total				\$66k	

4.3 Exploring the Potential of 5D High-Granularity for Background Rejection

Additionally, we have plans to conduct simulation studies aimed at refining the FDC design. These simulations will involve comprehensive evaluations of the FDC capabilities for tagging converted electrons/photons, hadrons, and beam-gas for background rejection. Our objective is to develop algorithms that take into account the transverse, longitudinal, and temporal dimensions. It is worth noting that the potential of SiPM-on-tile technology for PID has not been extensively explored thus far, as it has not been a priority for CALICE/CEPC, except for test-beam contamination studies.

To evaluate its complete potential for PID, we will use 5D tagging with AI/ML approaches, benefiting from the expertise of our group. Currently, we are involved in an AI project funded by DOE-NP in collaboration with LBNL and LLNL, and the insights gained from this project are highly relevant to the present study. Specifically, we will conduct studies of classification and regression employing state-of-the-art point-cloud networks, which are capable of accommodating high dimensionality and complex geometries in a straightforward manner. To carry out these simulations, we will use our group's GPU workstation, equipped with four NVIDIA RTX 3090 cards.

4.4 Deliverables and Intermediate Milestones

Our plan for the period of October 2023 to September 2024 consists of the following deliverables (numbered) and intermediate milestones (bullets):

1) Finalize the design of the FDC based on SiPM-on-tile technology, guided by full simulations.
   - Define the tradeoff between sampling fraction (to improve energy resolution) and Moliere radius (to increase acceptance).
   - Determine the optimal granularity per layer to enhance rejection of converted-photon, hadron and beam-gas backgrounds.
   - Incorporate the design of the timing layer or pre-shower system into the FDC design.
2) Fully characterize scintillator strips and SiPMs, and define design parameters.
   - Perform light yield measurements using cosmic rays and a Sr-90 source.
   - Characterize uniformity using a Sr-90 source.
   - Measure time resolution and its dependence on light yield using a picosecond laser.

- Iterate the above steps, varying strip geometry, width, and SiPM size.

3) Construct a prototype of the detector that will be ready for beam testing.
   - Complete and test the procedure for scintillator strip machining.
   - Define the assembly procedure per layer, including ESR wrapping and SiPM soldering.
   - Calibrate each layer using cosmic rays.

4) Conduct a beam test of the prototype and analyze the results.
   - Transport the prototype to JLab Hall-D for testing.
   - Complete beam test run.
   - Analyze the collected data.

5) Submit a design paper and present the results at conferences.

4.5 Budget

Table 5 presents our budget for different funding scenarios. In addition to the materials required for the initial FDC prototype, we are seeking partial funding to support a graduate student at UCR, totaling 4 months full-time-equivalent, including salary, benefits and tuition costs. This student will be responsible for conducting test-bench measurements and simulation studies. The student will be supervised Prof. Arratia. Additionally, we request travel funds to enable the student's participation in the planned test at JLab.

Table 5: Budget with various scenarios. These numbers include the 55% UC overhead rate.

Material	Description	100%	80%	60%
Prototype materials	as per Table 4	\$102k	\$75k	\$60k
UCR grad student	4 months FTE	\$30k	\$30k	\$18k
UCR travel	Trip to JLab	\$2.5k	\$2.5k	\$2.5k
Total		\$135k	\$108k	\$81k

With a reduced budget of 80%, we would decrease the number of prototype layers to lower the overall cost while maintaining nominal graduate student support. In this scenario, we would still achieve all milestones, but the resulting smaller prototype will have incomplete longitudinal coverage, leading to potential leakage issues. If the budget is further reduced to 60%, we would need to reduce graduate student support, which would result in excluding the milestones related to simulation studies for background rejection from the scope of the proposal.

4.6 Cost Effectiveness

The SiPM-on-tile technology offers several appealing features, including a robust supply chain and a straightforward construction method. Scintillator material can be obtained from Eljien, a Texas-based supplier, and can be machined in any university machine shop. Additionally, emerging capabilities in injection molding from FNAL can significantly reduce the cost of scintillator strips (with dimples). Tungsten plates can readily be purchased from US suppliers. SiPMs, on the other hand, can be purchased from various reliable vendors like HPK, and PCBs can be ordered from a number of websites. Moreover,

the assembly process itself can be distributed among multiple institutes with minimal infrastructure requirements.

The cost of this technology is highly attractive, with SiPMs available at a bulk price of approximately \$7 per unit. Additionally, the cost of the HGROC ASIC allows for bias and readout at a rate of \$1 per channel, which is orders of magnitude smaller than it was just a few years ago.

While this proposal aims to explore and develop SiPM-on-tile technology for the FDC, these advancements could potentially have an impact on other EIC calorimeters that would benefit from a highly granular approach. Examples of such systems include the far-backward electron taggers, an ECAL insert in the hadron endcap, the ZDC, the B0 ECAL, and other similar systems.

4.7 Diversity, Equity, and Inclusion

Our group is actively engaged in the DOE-NP RENEW traineeship program, collaborating with various institutions to promote inclusivity, particularly among first-generation and low-income students. It is worth noting that UCR is a Minority-Serving Institution where 70% of our undergraduate students identify as members of ethnic minorities, the majority of which come from working class families. Additionally, UCR was ranked the top three institution in the nation for graduating the highest number of Hispanic-American students in STEM fields [32].

We will leverage our participation in the ongoing program and the supportive institutional environment at UCR to engage undergraduate students in various aspects of this project. Through the California EIC consortium, which hosts conferences biannually, students will be able to present their work, further enhancing their research experience and fostering a strong sense of community. To recruit students and provide effective mentoring, we will use proven methods that we have developed through our RENEW experience. We do not require funds to cover salaries for undergraduates involved in this project because they will supported by other active grants.

5 Summary and Conclusions

We have outlined the design of a small electromagnetic calorimeter called the Few-Degree Calorimeter (FDC) that would cover the range of $-4.6 < \eta < -3.6$. The purpose of this detector is to tag electrons at Q^2 ranging from 0.1 to 1.0 GeV^2, enabling future research on the transition to perturbative QCD and the gluon-saturation regime.

Our proposal addresses an emerging and urgent need recognized by the EIC community, as highlighted in the summary of the recent second-detector workshop, which included a list of "golden channels" that included the probing of *"F_2 at low x and Q^2"* and required the *"maximization of Q^2 tagger down to 0.1 GeV^2"* [33].

Our proposal aims to bring in the latest advances in SiPM-on-tile calorimetry to create a modern and improved version of the ZEUS Beam-Pipe Calorimeter and H1 Very Low Q^2 calorimeter, which bridged the Q^2 gap at HERA. The high-granularity 5D shower (position, time, and energy) measurements this technology provides can significantly enhance performance for identifying backgrounds such as hadrons, converted-photon and beam-gas events.

SiPM-on-tile technology has undergone significant improvements in recent years and has become one of the cornerstones of state-of-the-art calorimetry. It is backed by an active global community involved in various experiments at the LHC, ILC, CEPC, and other facilities. However, its development for generic R&D purposes at the EIC has been overlooked. This represents a missed opportunity that we aim to rectify.

A broad objective of this proposal is to bring in and further develop the SiPM-on-tile technology for electromagnetic calorimetry applications at the EIC. This builds upon the experience of our team, who recently proposed a SiPM-on-tile HCAL insert for ePIC. The proposed design for the FDC leverages our experience in various areas, including design, simulation, extensive bench-test characterization, and prototyping.

Additionally, our proposal aims to develop potential solutions that foster complementarity between ePIC and Detector 2. While investigating the feasibility of integrating an FDC into either ePIC or Detector 2, the latter option appears to offer more opportunities for optimization. This is due to the larger crossing angle envisioned for IP8, resulting in a greater gap in the crystal ECAL acceptance.

In summary, this document presents a concrete design with the potential to close the Q^2 gap while maintaining a compact and cost-effective solution using state-of-the-art ECAL technology. We will pursue a program to demonstrate the FDC concept and conduct initial beam tests. Our objective is to establish the groundwork that will stimulate new advancements in detector layout, enabling the exploration of fundamental EIC science while providing alternative options for complementarity with the second detector.

References

[1] R. Abdul Khalek et al. Science Requirements and Detector Concepts for the Electron-Ion Collider: EIC Yellow Report. *Nucl. Phys. A*, 1026:122447, 2022.

[2] EIC Detector Geometry Interaction Point 6 (version January 2023) ePIC-Detector.skp. https://eic.jlab.org/Geometry/Detector/Detector-20230108185912.html. Accessed: 2023-06-18.

[3] Elke-Caroline Aschenauer. Private communication. Unpublished.

[4] Global Detector Integration Working Group Meeting, Low Q^2 Coverage of ePIC (Monday 6 Feb 2023). https://indico.bnl.gov/event/18161/. Accessed: 2023-06-15.

[5] TWiki: Electron-Ion Collider Detectors, EEEMCal. https://wiki.jlab.org/cuawiki/index.php/Electron-Ion_Collider_Detectors:_EEEMCal. Accessed: 2023-06-18.

[6] Bernd Surrow, Physics at low Q^2 (May 17th 2023). https://indico.bnl.gov/event/18414/contributions/76079/. Accessed: 2023-06-15.

[7] Paul Newman "Inclusive Processes - Low Q^2 Reach" (Monday 6 Feb 2023). https://indico.bnl.gov/event/18161/#5-inclusive-processes-low-q2-r. Accessed: 2023-06-15.

[8] Bernd Surrow. Measurement of the proton structure function F_2 at low Q^2 and very low x with the ZEUS beam pipe calorimeter at HERA. *Eur. Phys. J. direct*, 1(1):2, 1999.

[9] A Stellberger, J Ferencei, F Kriváň, K Meier, O Niedermaier, O Nix, K Schmitt, J Špalek, J Stiewe, and M Weber. The VLQ calorimeter of H1 at HERA: a highly compact device for measurements of electrons and photons under very small scattering angles. *Nuclear Instruments and Methods in Physics Research Section A: Accelerators, Spectrometers, Detectors and Associated Equipment*, 515(3):543–562, dec 2003.

[10] J. Breitweg et al. Measurement of the proton structure function F_2 and $\sigma_{tot}^{\gamma^* p}$ at low Q^2 and very low x at HERA. *Phys. Lett. B*, 407:432–448, 1997.

[11] A. M. Staśto, K. Golec-Biernat, and J. Kwieciński. Geometric scaling for the total $\gamma^* p$ cross section in the low x region. *Phys. Rev. Lett.*, 86:596–599, Jan 2001.

[12] A. Aktas et al. Elastic J/psi production at HERA. *Eur. Phys. J. C*, 46:585–603, 2006.

[13] S. Chekanov et al. Exclusive ρ^0 production in deep inelastic scattering at HERA. *PMC Phys. A*, 1:6, 2007.

[14] H. Kowalski, T. Lappi, and R. Venugopalan. Nuclear enhancement of universal dynamics of high parton densities. *Phys. Rev. Lett.*, 100:022303, Jan 2008.

[15] EEEMCal, (Electron Ion Collider - EIC) Mechanical design and Integration. Version 1.2 . https://wiki.jlab.org/cuawiki/images/e/e5/EEEMCAL_Mechanical_design_2.pdf. Accessed: 2023-06-18.

[16] Felix Sefkow, Andy White, Kiyotomo Kawagoe, Roman Pöschl, and José Repond. Experimental Tests of Particle Flow Calorimetry. *Rev. Mod. Phys.*, 88:015003, 2016.

[17] Frank Simon. Silicon photomultipliers in particle and nuclear physics. *Nucl. Instrum. Meth. A*, 926:85–100, 2019.

[18] K. Francis et al. Performance of the first prototype of the CALICE scintillator strip electromagnetic calorimeter. *Nucl. Instrum. Meth. A*, 763:278–289, 2014.

[19] J. Repond et al. Construction and Response of a Highly Granular Scintillator-based Electromagnetic Calorimeter. *Nucl. Instrum. Meth. A*, 887:150–168, 2018.

[20] Katsushige Kotera, Daniel Jeans, Akiya Miyamoto, and Tohru Takeshita. A novel strip energy splitting algorithm for the fine granular readout of a scintillator strip electromagnetic calorimeter. *Nuclear Instruments and Methods in Physics Research Section A: Accelerators, Spectrometers, Detectors and Associated Equipment*, 789:158–164, 2015.

[21] Yong Liu at CEPC Physics and Detector Plenary Meeting, June 14th 2023 . https://indico.ihep.ac.cn/event/19954/contributions/135608/. Accessed: 2023-06-26.

[22] Mingyi Dong et al. CEPC Conceptual Design Report: Volume 2 - Physics & Detector. 11 2018.

[23] M. Y. Dong. R&D of the CEPC scintillator-tungsten ECAL. *JINST*, 13(03):C03024, 2018.

[24] Yazhou Niu et al. Design of Sc-ECAL prototype for CEPC and performance of first two layers. *JINST*, 15(05):C05036, 2020.

[25] Teresa Monteiro. *Study of exclusive electroproduction of ρ^0 mesons at low Q^2 using the ZEUS Beam Pipe Calorimeter at HERA*. PhD thesis, Hamburg U., 1998.

[26] Ferdinand Willeke and J. Beebe-Wang. Electron Ion Collider Conceptual Design Report 2021. 2 2021.

[27] Miguel Arratia, Luis Garabito Ruiz, Jiajun Huang, Sebouh J. Paul, Sean Preins, and Miguel Rodriguez. Studies of time resolution, light yield, and crosstalk using SiPM-on-tile calorimetry for the future Electron-Ion Collider. *JINST*, 18(05):P05045, 2023.

[28] Miguel Arratia et al. A high-granularity calorimeter insert based on SiPM-on-tile technology at the future Electron-Ion Collider. *Nucl. Instrum. Meth. A*, 1047:167866, 2023.

[29] Fabian Hummer, Lorenz Emberger, and Frank Simon. Exploring the intrinsic time resolution of the SiPM-on-tile technology, 2022. DPG Spring Meeting.

[30] Wataru Ootani "Sc-ECAL R&D plan @ Japan" (Oct 2022). . https://agenda.linearcollider.org/event/9076/timetable/?view=standard#50-flash-talks-and-discussion. Accessed: 2023-07-11.

[31] Joel N. Butler and Tommaso Tabarelli de Fatis. A MIP Timing Detector for the CMS Phase-2 Upgrade. 2019.

[32] NSF's National Center for Science and Engineering Statistics. Women, minorities, and persons with disabilities in science and engineering. https://ncses.nsf.gov/pubs/nsf19304/digest/about-this-report in tables 5-12, 2019.

[33] Thomas Ullrich "Summary slides at the 1st International Workshop for a Second Detector at the EIC" (May 17th). https://indico.bnl.gov/event/18414/sessions/6192/#20230519. Accessed: 2023-06-16.